

High-performance self-powered photodetector based on organic/inorganic hybrid van der Waals heterojunction of rubrene/silicon

Yancai Xu(徐彦彩), Rong Zhou(周荣), Qin Yin(尹钦), Jiao Li(李娇), Guoxiang Si(侣国翔), and Hongbin Zhang(张洪宾)

Citation: Chin. Phys. B, 2021, 30 (**7**): 077304. DOI: 10.1088/1674-1056/abf345
Journal homepage: http://cpb.iphy.ac.cn; http://iopscience.iop.org/cpb

What follows is a list of articles you may be interested in

High-responsivity solar-blind photodetector based on MOCVD-grown Si-doped β-Ga_2O_3 thin film

Yu-Song Zhi(支钰崧), Wei-Yu Jiang(江为宇), Zeng Liu(刘增), Yuan-Yuan Liu(刘媛媛), Xu-Long Chu(褚旭龙), Jia-Hang Liu(刘佳航), Shan Li(李山), Zu-Yong Yan(晏祖勇), Yue-Hui Wang(王月晖), Pei-Gang Li(李培刚), Zhen-Ping Wu(吴真平), and Wei-Hua Tang(唐为华)

Chin. Phys. B, 2021, 30 (**5**): 057301. DOI: 10.1088/1674-1056/abe37a

Digital and analog memory devices based on 2D layered MPS_3 (M=Mn, Co, Ni) materials

Guihua Zhao(赵贵华), Li Wang(王力), Xi Ke(柯曦), and Zhiyi Yu(虞志益)

Chin. Phys. B, 2021, 30 (**4**): 047303. DOI: 10.1088/1674-1056/abd397

High-performing silicon-based germanium Schottky photodetector with ITO transparent electrode

Zhiwei Huang(黄志伟), Shaoying Ke(柯少颖), Jinrong Zhou(周锦荣), Yimo Zhao(赵一默), Wei Huang(黄巍), Songyan Chen(陈松岩), and Cheng Li(李成)

Chin. Phys. B, 2021, 30 (**3**): 037303. DOI: 10.1088/1674-1056/abd46b

Self-powered solar-blind photodiodes based on EFG-grown (100)-dominant β-Ga_2O_3 substrate

Xu-Long Chu(褚旭龙), Zeng Liu(刘增), Yu-Song Zhi(支钰崧), Yuan-Yuan Liu(刘媛媛), Shao-Hui Zhang(张少辉), Chao Wu(吴超), Ang Gao(高昂), Pei-Gang Li(李培刚), Dao-You Guo(郭道友), Zhen-Ping Wu(吴真平), and Wei-Hua Tang(唐为华)

Chin. Phys. B, 2021, 30 (**1**): 017302. DOI: 10.1088/1674-1056/abc546

Intrinsic charge transport behaviors in graphene-black phosphorus van der Waals heterojunction devices

Guo-Cai Wang(王国才), Liang-Mei Wu(吴良妹), Jia-Hao Yan(严佳浩), Zhang Zhou(周璋), Rui-Song Ma(马瑞松), Hai-Fang Yang(杨海方), Jun-Jie Li(李俊杰), Chang-Zhi Gu(顾长志), Li-Hong Bao(鲍丽宏), Shi-Xuan Du(杜世萱), Hong-Jun Gao(高鸿钧)

Chin. Phys. B, 2018, 27 (**7**): 077303. DOI: 10.1088/1674-1056/27/7/077303

High-performance self-powered photodetector based on organic/inorganic hybrid van der Waals heterojunction of rubrene/silicon*

Yancai Xu(徐彦彩), Rong Zhou(周荣), Qin Yin(尹钦),
Jiao Li(李娇), Guoxiang Si(侣国翔), and Hongbin Zhang(张洪宾)†

School of Physics and Electronics, Shandong Normal University, Jinan 250014, *China*

(Received 3 March 2021; revised manuscript received 18 March 2021; accepted manuscript online 30 March 2021)

Organic/inorganic hybrid van der Waals heterostructure with an atomically abrupt interface has attracted great research interests within the field of multifunctional electronic and optoelectronic devices. The integration of organic rubrene films with inorganic Si semiconductors can avoid the atomic mutual-diffusion at the interface, and provide the possibility of forming two-dimensional van der Waals heterojunction accompanied with the type-Ⅱ energy band alignment, due to the transfer behaviors of majority carriers at the interface. In this study, the high-quality rubrene/Si van der Waals heterostructure with an electronically abrupt junction was prepared, and a self-powered photodetector was then constructed based on this hybrid heterojunction. The photodetector demonstrated an excellent switching response to the 1064 nm monochromatic light with large on/off current ratio of 7.0×10^3, the maximum photocurrent of 14.62 mA, the maximum responsivity of 2.07 A/W, the maximum detectivity of 2.9×10^{11} Jones, and a fast response time of 13.0 μs. This study offers important guidance for preparing high-quality rubrene/Si hybrid van der Waals heterostructure with desirable band alignment, and the designed heterojunction photodetector has an important application prospect in the field of multifunctional optoelectronics.

Keywords: rubrene, van der Waals heterojunction, photodetector, band alignment

PACS: 73.40.Lq, 85.60.Gz, 81.05.Fb, 73.25.+i **DOI:** 10.1088/1674-1056/abf345

1. Introduction

The high-quality two-dimensional semiconductor heterostructures represent the essential material foundation for the state-of-the-art microelectronics and optoelectronics, which open up new opportunities for novel device applications as well as fundamental studies.[1–7] Among the various heterostructure integration strategies, the van der Waals integration becomes more favorable for creation of two-dimensional functional heterostructures with high-quality interfaces, because it can physically assemble the highly disparate materials together through the weak van der Waals interaction without lattice and processing limitations.[8–13] Thus, due to no requirements of synthesis compatibility, the current van der Waals integration is more flexible on selection of lattice structures of different materials compared to the traditional growth methods, and it has great potential for creating two-dimensional artificial heterostructures with pristine and electronically sharp interfaces beyond the scope of existing heterostructural materials.[6,14,15] Compared to the conventional inorganic semiconductor heterostructures, the emerging two-dimensional organic/inorganic hybrid van der Waals heterojunction offers the more perfect platform for the energy-band alignment engineering between the organic and inorganic semiconductors, and helps to realize more efficient heterostructure optoelectronic devices with new functionalities.[8,16–18] The inorganic semiconductors usually have a larger carrier mobility yet higher growth temperatures, while the organics are generally characterized by greater flexibility and lower growth temperatures.[19–22] On the other hand, the conventional inorganic semiconductors usually rely on the high-energy vaporization processes, which usually involves continuous bombardment, clusters, and strong local heating in the contact region by high-energy atoms. This feature can produce a typical and disordered glassy layer at the heterostructure interfaces, leading to the incontrollable Fermi level pinning effect inside the devices.[1] As a consequence, the integration of organic/inorganic hybrid van der Waals heterojunctions can avoid the atomic mutual-diffusion at interfaces, and would facilitate to form an atomically sharp interface, which is conducive to the realization of an electronically abrupt junction. In addition, the organic/inorganic hybrid van der Waals heterojunction is very beneficial for many photophysics processes on the interface, including photoexcited electron generation, interfacial carrier transfer, and so on, which can be utilized for the construction of multifunctional photonic and optoelectronic devices with higher external quantum efficiency.[17]

Among various organic semiconductors, the organic

*Project supported by the National Natural Science Foundation of China (Grant Nos. 11604228, 11774208, and 11974222), the Science and Technology Planning Foundation of Shandong Province, China (Grant No. J18KA219).

†Corresponding author. E-mail: hbzhang@sdnu.edu.cn

© 2021 Chinese Physical Society and IOP Publishing Ltd

rubrene (5,6,11,12-tetraphenyltetracene) crystal has been attracting tremendous research interest from both fundamental and application viewpoints.[23–25] The organic rubrene crystal usually exhibits the largest hole mobility (μ_h) of 40.0 $cm^2 \cdot V^{-1} \cdot s^{-1}$, which is traced back to the light effective mass and delocalized nature of the holes in the highest occupied molecular orbital (HOMO) of rubrene crystal.[23,25–27] In theory, integration of such an organic rubrene crystal with traditional Si semiconductor can provide the possibility of forming a high-quality organic/inorganic van der Waals heterostructure with the type-Ⅱ (staggered) band alignment due to the transfer behaviors of majority carriers on the interface.[28,29] Furthermore, the interlayer electron excitons can be realized in this organic/inorganic hybrid heterostructure of rubrene/Si with much longer lifetime because of the type-Ⅱ band alignment configuration. After higher light absorption, a large number of photoexcited carriers will be generated and transfer across the rubrene/Si interface. The result is that the photoexcitation electrons and holes may be separated at different layers between the rubrene film and Si wafer due to their band structure offset. This feature indicates the great potential of the rubrene/Si heterostructure for light harvesting and photodetection applications, however, the desired optical and optoelectronic devices based on this layered organic/inorganic hybrid van der Waals heterojunction of rubrene/Si have not been studied experimentally so far. In this study, the high-quality organic/inorganic hybrid and vertical van der Waals heterostructures of rubrene/Si were prepared based on the p-type rubrene crystal films and n-type Si wafers with a greater rectifying ratio up to 400. A self-powered photodetector was then designed based on this fabricated van der Waals heterojunction, which demonstrated the ultrafast and highly-sensitive photoelectric response to the incident 1064 nm light with large photocurrent up to 14.62 mA. This study has important guiding significance for preparing high-quality rubrene/Si hybrid heterostructure with desirable band alignment, and it also provides a novel material platform for fabrication of multifunctional heterojunction photodetectors.

2. Results and discussions

The typical structure diagram of rubrene molecules is demonstrated in Fig. 1(a), which comprises of a tetracene backbone core accompanied symmetrically with two pairs of phenyl substituents on either side of the backbone. As a matter of fact, there exist two conformations of the rubrene molecules, i.e., the planar rubrene molecule and the twisted rubrene molecule which possesses a twisting tetracene-backbone of ∼42°.[30,31] In this work, the organic rubrene crystal films were prepared by physical vapor deposition technology in the tube furnace, as shown in Fig. 1(b). The rubrene powder with purity of greater than 98.0% was adopted as the evaporation precursor to grow the organic crystalline rubrene films. The cleaned and monocrystalline Si wafers were used as the growth substrate, which is away from the heat center of the quartz tube about 15 cm. Before the sample growth, the high-purity argon (Ar) gas was used to flush the quartz tube for several times for elimination of oxygen contamination, and the cavity of the quartz tube was finally maintained at the background gas pressure of 7.0×10^{-1} Pa. During the growth of rubrene films, the precursor powder was heated to 300°C with a working gas pressure of 20 Pa and a constant argon flow of 30 sccm. The thickness of rubrene films can be controlled by means of adjusting the evaporation time, and it was controlled for an hour in this study. The as-grown rubrene films cooled down to room temperature were finally taken out from the quartz tube, and prepared for further physical and electrical characterizations. Figure 1(c) shows the typical growth morphology of the surface of rubrene films, which was investigated by means of SEM. The rubrene film has a relatively smooth surface on the whole, although some crystalline droplets and needles occur on the upper surface of the film, and the observed morphology of the rubrene films is also consistent with the typical morphologies of rubrene films reported in the literature.[32] The cross-section image characterized by SEM shown in Fig. 1(d) also confirmed that the as-grown rubrene film has a uniform thickness about 600 nm.

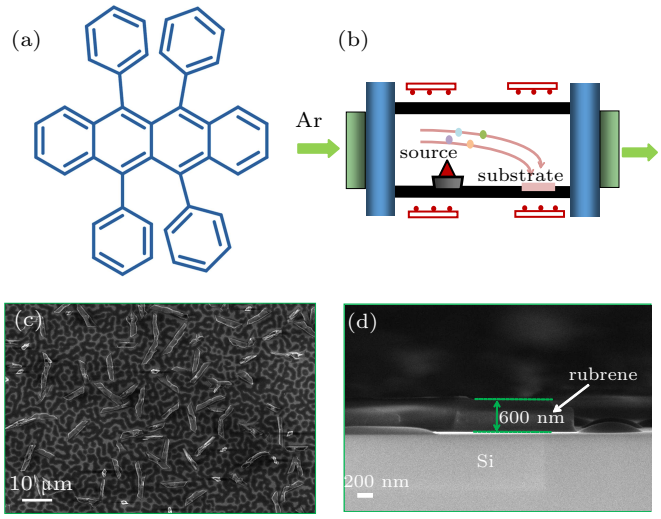


Fig. 1. (a) Schematic diagram of rubrene molecule. (b) Schematic diagram of the van der Waals epitaxial growth apparatus. (c) Representative SEM morphology of the surface of the as-grown rubrene films. (d) The cross-section image of the rubrene film characterized by SEM.

The crystallinity property and molecular configuration of the rubrene films prepared on silicon substrates were then investigated by the XRD and FTIR, as described in Figs. 2(a) and 2(b), respectively. The obtained characteristic diffraction peaks in the XRD pattern of films were sharp and intense, indicating the higher crystalline nature of the rubrene films with a face-centered orthorhombic structure. The lattice parameter of

the orthorhombic rubrene is of $a = 2.686$ nm, $b = 0.719$ nm, and $c = 1.443$ nm at room temperature.[23,31,33] The diffraction peaks at $2\theta = 6.63°$, 14.1°, 19.7°, and 25.1° are corresponding to the (200), (400), (600) and (800) planes of the orthorhombic rubrene crystal.[31,33] Moreover, the measured diffraction peaks at $2\theta = 12.21°$, 16.92°, 17.65°, 22.43°, and 27.69° correspond to the (002), (311), (112), (113) and (022) planes of the orthorhombic rubrene as well, which is consistent with the reported literature.[23,33] The FTIR investigation also observed the significant characteristic vibration peaks of the rubrene molecular, as shown in Fig. 2(b). The skeletal vibration of ring of rubrene molecules results in five characteristic peaks located at 1590, 1530, 1491, 1440 and 1384 cm^{-1}. In addition, the sharp peaks located at 3016, 3052 and 2910 cm^{-1} should be due to the aromatic C–H stretching of the rubrene crystal.[34] The peaks at 1027, 914, 760, 689 and 661 cm^{-1} are due to the vibrations of the aromatic ring.[35] Furthermore, the observed peaks at 2034 and 2162 cm^{-1} should be attributed to the vibration of Si–H group bonds which come from the surface of the Si substrate,[36–38] and the observed peak located at 2362 cm^{-1} should originate from the CO_2 stretch vibration of the air.[39] In order to reveal the overall light absorption characteristic for the as-prepared rubrene/Si heterostructure, we firstly measured the UV-vis absorption spectrum from the rubrene/Si heterojunction, as shown in Fig. 2(c). Note that the rubrene/Si heterostructure has a strong light absorption within the wavelength of 200 nm–650 nm. Further increase of the light wavelength results in a gradual decrease of light absorption, due to the decreasing photon energy. The photoluminescence characteristic of the as-grown rubrene films was then investigated, and the obtained typical PL spectrum of rubrene is shown in Fig. 2(d). The three characteristic PL peaks located at 1.88, 2.07, and 2.18 eV should be assigned to the twisted rubrene molecule, which matches well to those discussed early in literature.[31] The PL peak at 2.18 eV should be identified as Frenkel exciton recombination process as mentioned in literature, and the energy of this peak was slightly smaller than the band-gap energy (E_g) of rubrene films by around 0.03 eV.[31,40] The other two peaks at 2.07 eV and 1.88 eV should be ascribed to the vibrational progressions from the first and the second vibrational energies of the ground singlet S_0 state of a twisted rubrene molecule, respectively.[31] As a special kind of local molecular excited state, the Frenkel exciton is commonly observed in organic molecular semiconductors, which belongs to an electrically neutral quasiparticle and consists of an electron and hole pair.[41] These excitons usually diffuse inside the organic semiconductor before recombination, and then be trapped in the low energy region near the defects, impurities or grain boundary.[31] As a result, the PL spectrum of the rubrene crystal induced by the Frenkel excitons usually accompanies by vibronic lines originated from molecular orbitals and vibrations.[41] Therefore, through these detailed physical characterizations, we can confirm that the as-grown rubrene films on the Si substrate have a higher crystal property and should be constituted by the twisted rubrene moleculars with orthorhombic structure.

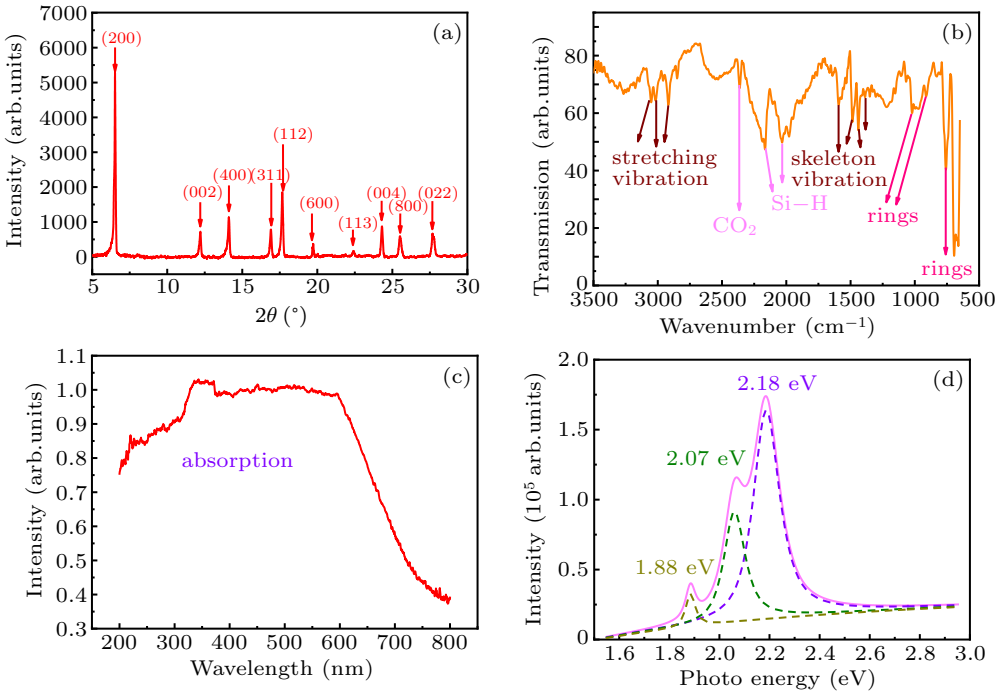


Fig. 2. (a) XRD pattern of the as-grown rubrene crystalline films. (b) Representative fourier transform infrared spectroscopy (FTIR) of rubrene crystalline films. (c) UV-vis absorption spectrum of the as-grown rubrene/Si heterostructure. (d) The typical photoluminescence spectrum of the rubrene crystalline films.

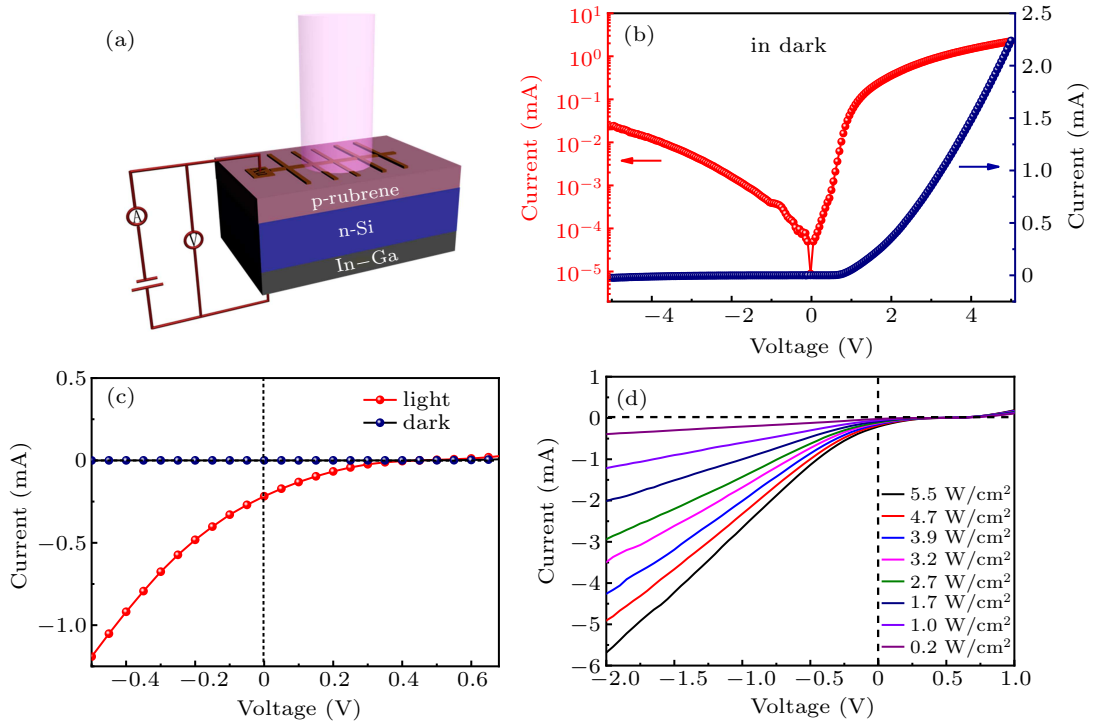


Fig. 3. (a) Diagrammatic drawing of the rubrene/Si hybrid heterojunction devices. (b) The measured *I*–*V* characteristic curve under dark with linear (right) and semi-logarithmic (left) coordinates. (c) Photocurrent response of the detector to the 1064 nm monochromatic light. (d) The measured *I*–*V* curves of the device under different intensities of the 1064 nm light. All the *I*–*V* curves were measured at room temperature.

Based on the prepared high-quality rubrene/Si heterostructure, we fabricated the high-performance heterojunction photodetector as schematically shown in Fig. 3(a). The top surface of the rubrene film was deposited by an Au electrode with thickness about 60 nm via magnetron sputtering assisted with a shadow mask.[42] Because the highest occupied molecular orbital of rubrene is 5.36 eV, which is close to the work function of Au electrode (5.1 eV), the preparation of Au electrode is beneficial for formation of a good ohmic contact with the rubrene film. Meanwhile, the small difference between the two energy levels can facilitate the transfer of photogenerated holes from the rubrene film to the Au electrode. In addition, the In–Ga alloy was adopted as the other electrode material and pasted on the bottom of Si wafer. The bottom of the conduction band of Si is 4.05 eV, which is very close to the work function of In–Ga alloy (4.1–4.2 eV) as well. Therefore, the preparation of In–Ga alloy electrode on the bottom of Si can help to form a good ohmic contact, and be beneficial for the transfer of photogenerated electrons from the Si layer to the In–Ga electrode.[43] During the photoelectric characterization, the incident light generated by a 1064 nm laser can irradiate vertically to the surface of the device, whose spot area was focused slightly less than the surface area of the device of 0.20 cm^2. Figure 3(b) shows the representative current-voltage characteristic curve of the rubrene/Si heterojunction device within dark conditions in linear (right) and semi-logarithmic (left) coordinates. As shown in Fig. 3(b), the heterostructure device exhibits an obvious diode transport characteristic, and the current can flow through the device only under the forward bias voltages. Notably, the minimum dark current can reach the value as lower as 1.0×10^{-5} mA at 0 V, which is very beneficial to obtain a larger detectivity of the device. The rectifying performance of the heterostructure device is usually evaluated by the parameter of the rectifying ratio, which is normally defined as[43]

$$\text{ratio}(V) = \left|\frac{I(+V)}{I(-V)}\right| = \left|\frac{R(-V)}{R(+V)}\right|. \quad (1)$$

Here, $I(+V)$ and $R(+V)$ correspond to the forward current and resistance in the current-voltage characteristic curve, while the $I(-V)$ and $R(-V)$ correspond to the reverse current and resistance of the transport curve. By means of linearly fitting the *I*–*V* curve along the forward and reverse current directions, we can calculate that the rectification ratio of the device is equal to ∼400. It reveals that an electronically abrupt p–n heterojunction has been created between the organic rubrene crystal film and inorganic Si wafer, which is very conductive to fabricate the high-performance heterostructure photodetectors. The photoelectric conversion property of the device was subsequently investigated under the 1064 nm light illumination, as shown in Fig. 3(c). The heterostructure photodetector displays evident photocurrent response behavior, and the photocurrent is mainly produced in the direction of reverse bias voltages. Significantly, the heterostructure device showed the remarkable photovoltaic characteristic, and the open-circuit voltage can reach up to 0.3 V attributed to the effective electron-hole separation caused by the heterostructure band alignment. The evolution of the *I*–*V* curve as a function of the light intensity was further analyzed, as shown in Fig. 3(d). These *I*–*V*

curve characterizations reveal that the heterostructure device is very sensitive to the incident 1064 nm light, and the photocurrent curve increases monotonically as the intensity of light increases. The maximum photocurrent can reach as higher as 5.6 mA at 5.5 W/cm^2 and −2 V, and such a larger photocurrent can satisfy the demands of actual photonics applications.

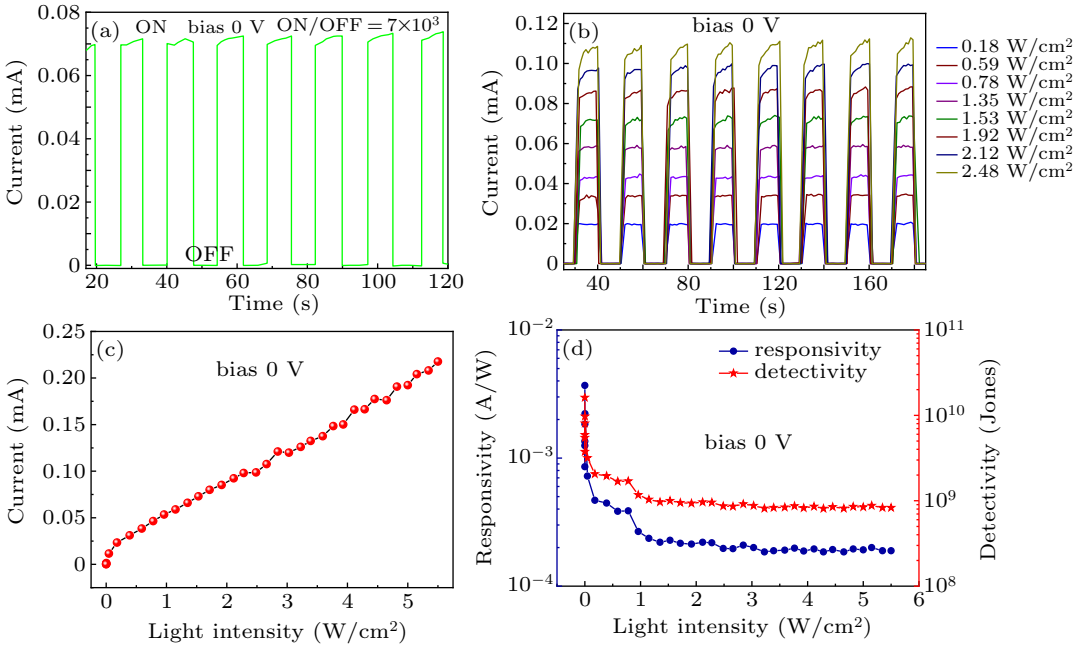


Fig. 4. (a) The switching response of the photocurrent to the 1064 nm light without any external voltages. (b) Photocurrent switching performance varying with the incident intensity of lights at zero voltage. (c) The photocurrent curve calculated from the switching data at zero voltage. (d) The calculated responsivity and detectivity curves varying with the incident intensity of lights under zero voltage, respectively.

The photocurrent switching characteristics were further investigated for our device working in zero bias mode, as illustrated in Fig. 4(a). It shows an excellent and stable switching performance with a lager photocurrent of 0.07 mA and a weaker dark-current value of 1.0×10^{-5} mA at 1.53 W/cm^2. Therefore, the on/off ($I_{\text{photo}}/I_{\text{dark}}$) ratio of the heterostructure photodetector can reach as high as 7.0×10^3 under zero bias. The photocurrent switch evolution of the detector operated in zero bias mode and under the irradiation of 1064 nm light with different intensities was also investigated as shown in Fig. 4(b). Notably, the incident intensity of lights has a strong impact on the amplitude of the photoelectric switch characteristic, which leads to a monotonous increase of photocurrent from 1.97×10^{-2} mA at 0.18 W/cm^2 to 0.109 mA at 2.5 W/cm^2. We then calculated the detailed photocurrent values from the measured switching original data under each selected values of the light intensity, and Fig. 4(c) provides the typical photocurrent versus light intensity. The value of photocurrent increases almost linearly with the increase of light intensity, especially under the higher light intensity radiation conditions. The obtained maximum photocurrent value is about 0.22 mA even under zero bias, which further confirms the high performance of our rubrene/Si heterostructure device. Additionally, the device performances are often evaluated through two significant parameters of responsivity (R) and detectivity (D^*). It is worth pointing out that the parameter of responsivity is normally defined as

$$R = I_{\text{photo}}/P_{\text{in}}, \tag{2}$$

which usually reflects a device's sensitivity to light signal.[43,44] The detectivity is usually used to evaluate the capability of a detector for detecting the tiny lights, and it is normally determined by the formula[44–46]

$$D^* = \frac{A^{1/2}R}{(2qI_{\text{dark}})^{1/2}}. \tag{3}$$

The parameter of I_{dark} in the formula has defined the dark current of the device. The parameter A is defined as the active area of the device, and the actual value of this parameter is about 0.20 cm^2. During measurements, the incident light is focused by a laser collimator, and the area of the spot was controlled compared to the area of the device, and the margin of error is less than 5%. By referring to these two formulas, the specific values of R and D^* were then calculated at different intensities of 1064 nm light, and Fig. 4(d) shows the corresponding R and D^* curves for our heterojunction device operated within self-driven mode. The photodetector usually has the larger light responsivity and detectivity under the lower light intensity, and they also become saturated in the stronger light-intensity situations. Note that the maximum light responsivity and detectivity of 3.7×10^{-3} A/W and 1.62×10^{10} Jones can be obtained under the self-driven condition, respectively. These excellent performance parameters demonstrated that the

rubrene/Si hybrid heterojunction device can also be applied to the self-driven detector, and there is almost no energy loss during the operation with zero bias voltage.

The bias-voltage dependence characteristic of the photoelectric conversion behavior of the rubrene/Si heterojunction photodetector was then studied as shown in Fig. 5 as well. Figure 5(a) shows the typical photocurrent switching data measured with different intensities of light and an external bias of −5 V. The measurements reveal that the current of the device can achieve the stable on/off states following with the incident light opening and closing. It is important that the switching behavior of the photodetector can be able to keep the excellent stability and invertibility with almost constant photocurrent values during each on/off states under fixed light intensity even in the case of applied bias voltages. Note that the photocurrent can reach a large value of 14.6 mA from 4.5 mA at the reverse bias of −5.0 V with increasing light intensity to 5.5 W/cm^2 from the 1.35 W/cm^2. The photocurrent curves calculated from the switching data at 0, −1.0, −2.0, −3.0, −4.0 and −5.0 V are shown in Fig. 5(b). It is worth noting that the photocurrent increases almost linearly in the whole range of light intensity at the five selected bias voltages. Furthermore, the photocurrent value increases obviously with the bias voltage rising, indicating the enhanced responsivity over the whole range of light intensity. The photocurrent value versus bias-voltage curve in the range of 0 to 5.0 V under the light illumination of 5.5 W/cm^2 is described in Fig. 5(c). The photocurrent increases rapidly within the lower bias voltage range, and turns to be saturated as the bias voltage increases greater than 3.0 V. Under each fixed light intensity, there exists a maximum and saturation value for the photogenerated electron-hole pairs for the rubrene/Si heterojunction. As a small bias voltage is applied, the additional potential can greatly improve the separation ability of photogenerated carriers, resulting in an increasing photocurrent effect. As the applied bias voltage increases greater than 3.0 V, the majority of the electron-hole pairs have been separated, and very limited photogenerated carriers can contribute to the observable photocurrent effect with increasing the external bias voltage, therefore, the measured photocurrent turns to be saturated. Finally, the value of photocurrent can be enhanced to 14.6 mA at −5.0 V from 0.22 mA at zero voltage. The responsivity and detectivity curves calculated from the switching data with different light intensities at 0, −1.0, −2.0, −3.0, −4.0 and −5.0 V are shown in Figs. 5(d) and 5(e), respectively. The R and D^* show a qualitatively consistent change law under each bias voltages, and they are very sensitive to the incident light with lower intensities due to the higher external quantum efficiency of the device. However, the R and D^* values tend to be saturation under the strong light-intensity conditions, due to the increased recombination effect of electron-hole pairs induced by the larger number of photo-excited carriers. The bias voltage dependent responsivity and detectivity curves obtained under the 1064 nm light illumination of 8.5×10^{-5} W/cm^2 are given in Fig. 5(f). The values of R and D^* increase monotonically with raising the reverse bias voltage gradually, and the maximum R and D^* of 2.07 A/W and 2.9×10^{11} Jones can be acquired at −5.0 V for our fabricated rubrene/Si heterojunction photodetector.

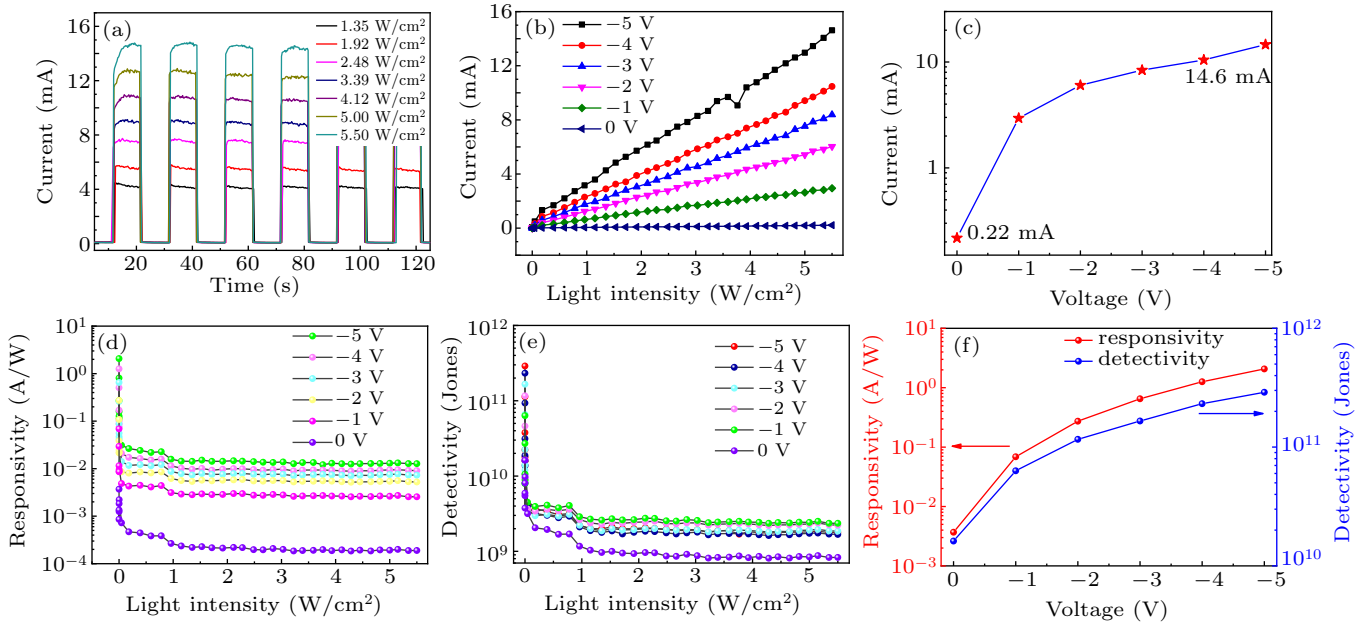


Fig. 5. (a) Light-intensity dependent switching data of the photocurrent measured under an external bias of −5.0 V and 1064 nm light. (b) The calculated photocurrent curves from the switching data at 0, −1.0, −2.0, −3.0, −4.0 and −5.0 V, respectively. (c) The photocurrent value curve with increasing bias voltages within the range from 0 to −5.0 V. The calculated responsivity (d) and detectivity (e) curves within the intensity of 1064 nm light range from 0 to 5.5 W/cm^2 at 0, −1.0, −2.0, −3.0, −4.0 and −5.0 V, respectively. (f) The bias-voltage dependences of the responsivity and detectivity of the detector, respectively.

In order to prove that the as-fabricated device can detect the light signals with higher frequencies, we then investigated the photovoltaic conversion characteristics of our device under the high frequency light illumination up to several thousands of Hz. During the process of experiment, an oscilloscope was used to detect the switching performance of the photovoltage (V_{oc}) of the photodetector. The wavelength of the light source used in the high-frequency measurements is 980 nm, and the incident intensity of the light is about 0.026 mW/cm^2. The frequency of the pulsed light was control by a signal generator. During measurements, a square-wave voltage signal with amplitude of 5.0 V was produced by the signal generator, which was used to drive a phototransistor to produce the high-frequency pulsed light, and the detailed frequencies of light signals were controlled by means of regulating the frequencies of the square-wave voltage signal. Figures 6(a) and 6(b) show the representative photovoltage switching characteristics with the pulsed light frequencies of 50 Hz (a) and 5.0 kHz (b). Obviously, the detector can exhibit a superfast and steadily photoelectric response to the pulsed light even on the high-frequency operating mode up to 5.0 kHz. As one of the key parameters to evaluate the performance of photodetectors, the characteristic rising (t_r) and falling (t_f) times of the switching data is normally used to characterize the response speed of the device.[43] From the high-resolution photovoltage switching data measured at the frequency of 5.0 kHz shown in Fig. 6(c), the response speed with $t_r = 13.00$ μs and $t_f = 110.0$ μs can be achieved, demonstrating a super fast response speed on the order of microseconds. The asymmetric rise and fall times of the photodetector may be due to the different carrier excitation and relaxation processes. The ultra-fast excitation of electron-hole pairs via absorbing photons often results in an ultra-fast rising edge, while the free relaxation process of photon-generated carriers often leads to the trailing phenomena along the falling edge. In addition, we also investigated the high-frequency switching performance of the photodetector that was kept in the atmosphere for about two months as demonstrated in Fig. 6(d). Note that the photovoltage of the device after long-term storage can keep close to the initial one, and there is almost no aging effect that can be observed, indicating the excellent device stability.

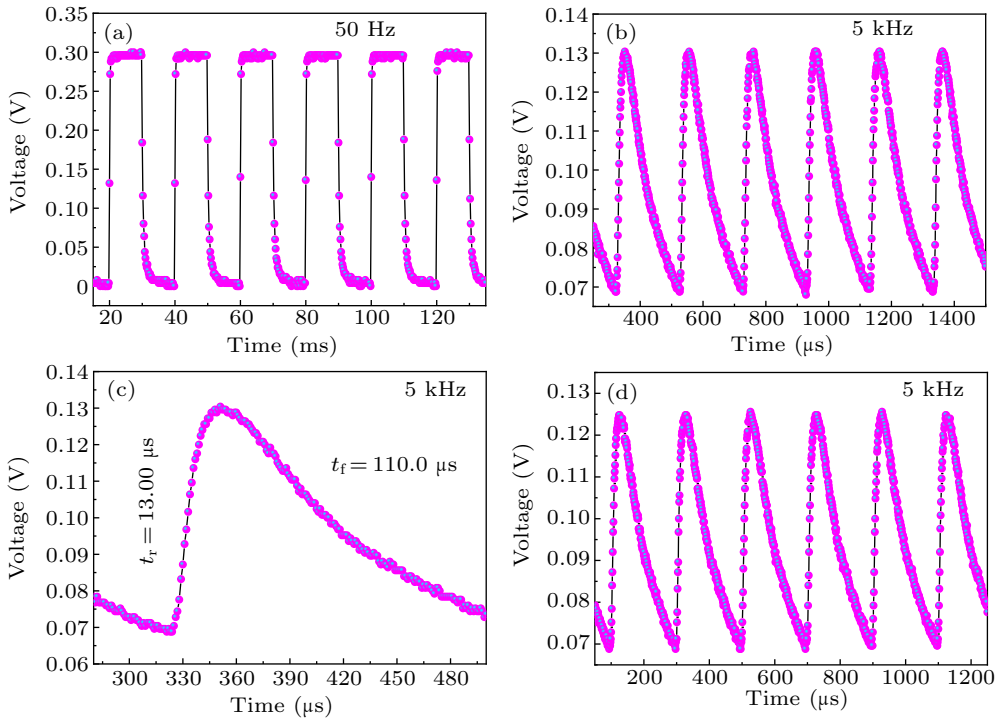


Fig. 6. (a) Photovoltage switching characteristic of the photodetector measured at 50 Hz. (b) High-frequency response of the photodetector at 5.0 kHz. (c) The detailed drawing of the photovoltage switching data with only one rising edge and one falling edge. (d) Photovoltage switching response of the photodetector after long-term storage in air at 5.0 kHz.

The response wavelength range of the device was also investigated within the measurable optical wavelength range of 300 nm–1100 nm. The fitting photocurrent (I_p), responsivity (R), detectivity (D^*), and external quantum efficiency (EQE) curves as a function of incident wavelengths are demonstrated respectively in Figs. 7(a), 7(b), 7(c), and 7(d). As shown in Fig. 7(a), the photocurrent grows quickly with increase in light wavelength to 900 nm from 300 nm, while it begins to gradually drop as the light wavelength further increases to 1100 nm. Therefore, the heterostructure photodetector always gets a maximum photocurrent value at the wavelength of 900 nm. In addition, the calculated R and D^* curves of the

heterojunction device demonstrate almost a uniform evolution rule with the variation of light wavelength, as illustrated by Figs. 7(b) and 7(c). Both of them can get a maximum value under the light illumination of 900 nm, which is consistent with the characteristic of the photocurrent. Within the wavelength range of 450 nm ~900 nm, the variation tendency of the responsivity and detectivity of the photodetector is relatively flat, and they decline slowly as the light wavelength decreases. However, when the light wavelength becomes less than 450 nm or more than 900 nm, the responsivity and detectivity turn to decline rapidly. We then analyzed the EQE properties of the device with the change of light wavelength, as shown in Fig. 7(d). The detailed values of the EQE are usually calculated using the equation[45,47]

$$\mathrm{EQE} = \frac{J_{\mathrm{photo}}/q}{P/h\nu} = R\frac{hc}{q\lambda}, \tag{4}$$

where the four parameters λ, c, ν, and h are the wavelength of lights, the velocity of lights, the frequency of photons, and Planck's constant, respectively. It is worth noting that almost constant EQE values were obtained for the device within the light wavelength range of 450 nm–900 nm, manifesting that the same number of photoexcited electron-hole pairs can be produced via absorbing one photon within this wavelength range. However, the EQE value of the photodetector reduces rapidly as the incident light goes out of this wavelength range. This suggests that the photocarriers can not be effectively generated as the light wavelength becomes less than 450 nm and more than 900 nm. In theory, the light intensity and photon energy must follow the formula:[48]

$$P = Nh\nu = Nh\frac{c}{\lambda}, \tag{5}$$

where N is the number of incident photon. This means that when the light intensity is consistent, the shorter the wavelength, the fewer photons there are. Therefore, as the incident lights with wavelengths in the range of 450 nm–900 nm illuminate on the surface of the device, the number of the photocarriers will be reduced with decreasing light wavelength at the same incident light intensity due to the decreased number of incident photons, although they have the same generation efficiency for photon-generated electron-hole pairs in this wavelength range. It also reveals the principle of the gradually decreased photocurrent, responsivity, and detectivity, when the light wavelength reduces from 900 nm to 450 nm, as shown in Figs. 7(a)–7(c). However, as the wavelength of the incident lights decreases below 450 nm, the absorption coefficient and penetration depth of the incident lights will gradually decrease with the wavelength declining. The number of electron-hole pairs induced by the optical excitation will be decreased inside the rubrene/Si heterostructure. The majority of optical-excitation carriers are generated in the upper layer of rubrene, and they cannot be effectively separated at the heterojunction interface, which may result in a very high recombination rate of photo-generated carriers inside the rubrene film. Therefore, this drawback leads to a rapid decrease in photocurrent, responsivity, detectivity and external quantum efficiency, when the wavelength of incident lights decreases from 450 nm to 300 nm.

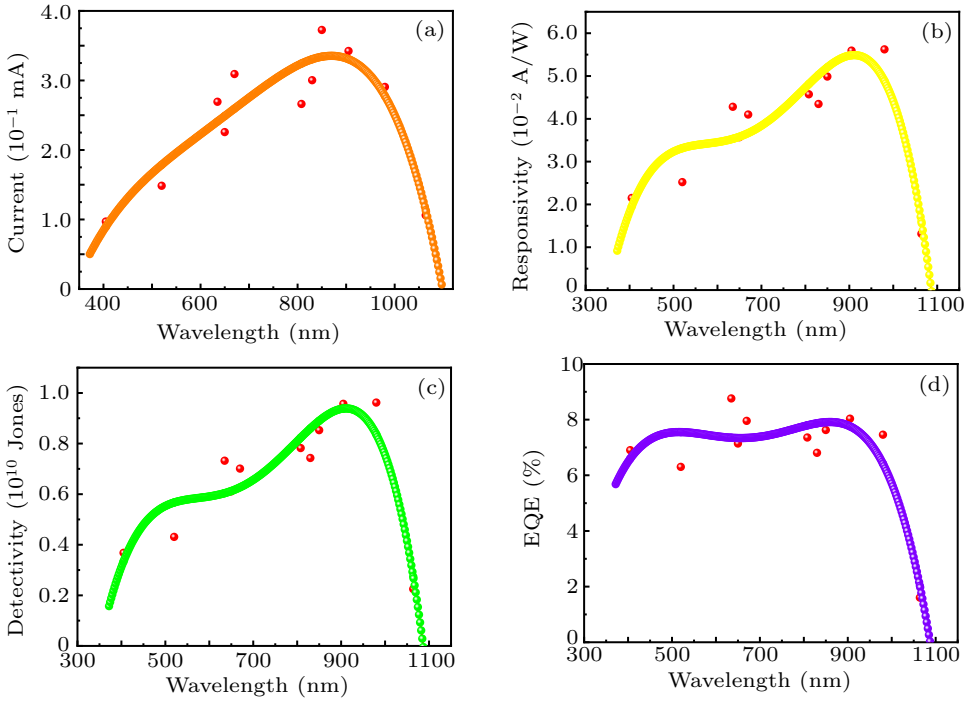


Fig. 7. The photocurrent (a), responsivity (b), detectivity (c), and external quantum efficiency (d) of the rubrene/Si hybrid heterojunction device as a function of light wavelengths from 300 to 1100 nm.

Table 1. Comparisons of characteristic parameters between the rubrene/Si hybrid van der Waals heterojunction photodetector with other rubrene-based devices in literature.

Materials and devices	Photocurrent (mA)	Responsivity (A/W)	Detectivity (Jones)	Working wavelength (nm)	Response time (t_r/t_f) (μs)	References
Rubrene/Si	14.62	2.07	2.9×10^{11}	1064	13.0/110.0	This work
Rubrene/fullerene	–	0.136	–	536	$1.8\times10^3/2.2\times10^3$	[49]
Orthorhombic rubrene nanowire FET	3.87×10^{-5}	687.0	–	450-750	–	[50]
MoS_2/rubrene-patch TFT	1×10^{-7}	0.326	–	455	–	[51]
Rubrene/graphene phototransistor	4×10^{-3}	10^7	9.2×10^{11}	500	–	[52]
Aniline-rubrene-gold nanocomposite TFT	1×10^{-5}	4.418×10^{-2}	2.15×10^{10}	520	–	[53]
ZnO nanobridge/rubrene	2.25×10^{-4}	8×10^{-3}	–	532	$0.8\times10^6/1.7\times10^6$	[54]

Furthermore, as the wavelength of incident lights increases higher than 900 nm, the photon energy of the incident lights will decrease gradually with the continuously increase of light wavelength. The lower photon excitation energy and weaker absorption coefficient can not effectively excite the electron-hole pairs inside the rubrene/Si heterostructure, especially as the photon energies become less than the forbidden gap (E_g) of the rubrene crystalline film. This feature finally results in a rapid reduction in external quantum efficiency of the photodetector with increase in light wavelength toward 1100 nm from 900 nm, and consequently the decrease of photocurrent, responsivity, and detectivity, as shown in Figs. 7(a)–7(d). Table 1 shows the comparison of the main parameters of the rubrene/Si hybrid heterojunction detector with other rubrene-based devices reported previously, which consists of the photocurrent, responsivity, detectivity, wavelength, and operating speed.[49–54] Note that the as-fabricated rubrene/Si heterojunction photodetector has the much higher photocurrent value as well as superfast operating speed, and they become larger than the reported ones with several orders of magnitude. Meanwhile, it also shows the relatively better responsivity, detectivity, as well as response wavelength compared to the previous devices, and can achieve an optimal balance among these important parameters. This result means that the designed rubrene/Si hybrid van der Waals heterojunction photodetector is more conducive to the practical applications of multifunctional optoelectronic devices.

To analyze the band structure characteristic of the as-prepared rubrene film, we then measured the UV-vis absorption spectrum from the rubrene film prepared on the quartz substrate, as shown in Fig. 8(a), in order to eliminate the light absorption effect of the substrate. Three characteristic peaks with energy of 2.36 eV, 2.52 eV, and 2.68 eV were observed in the UV-vis absorption spectrum of rubrene films. The characteristic peak located at 2.36 eV should originate from the electron transition of a twisted rubrene molecule, whose electrons can transfer to the first excited S_1 singlet state from the ground S_0 singlet state. The other two peaks at 2.52 eV and 2.68 eV could be attributed to the vibrational progression energies for the S_1 state.[30,31] The optical band gap (E_g) value of the rubrene films can be calculated using the equation[55]

$$(\alpha h\nu)^2 = B(h\nu - E_g), \tag{6}$$

where α, $h\nu$ and B are the light absorption coefficient, the photon energy, and a constant, respectively. In the data procession, we fit linearly the absorption threshold of the UV-vis spectrum as shown in Fig. 8(a), the energy value of $E_g = 2.21$ eV was determined experimentally, which matched well to those reported previously in the literature.[31,56] According to our experimental analysis as well as relevant literature reports, the band-structure diagram between the rubrene film and the silicon wafer was described in Fig. 8(b). The energy level of HOMO in the band diagram with energy of 5.36 eV represents the highest occupied orbital of rubrene molecular, while the LUMO with energy of 3.15 eV represents the lowest unoccupied orbital of rubrene molecular.[40,56,57] The E_C in the band diagram with energy of 4.05 eV represents the bottom energy level of the conduction band of silicon wafer, while the E_V with energy of 5.17 eV represents its top edge of valence band.[58] Furthermore, the E_F is defined as their corresponding Fermi energy levels. When the p-type rubrene crystal films are deposited onto the n-type Si substrates, their majority carriers will diffuse with each other due to the difference of energy levels, therefore, a large built-in electrical field and potential barrier can be formed at their interface under thermal equilibrium condition. After the heterostructure has grown, the corresponding band alignment of the rubrene/Si heterostructures will occur, as shown in Fig. 8(c), which should be ascribed to the type-Ⅱ (staggered) band alignment. The thicknesses of the rubrene film and Si wafer are about 600 nm and 350 μm for the constructed heterojunction device, respectively. The width of the space charge region of the heterojunction was estimated by the formula[59]

$$W = X_N + X_P = \left[\frac{2\varepsilon_n\varepsilon_p\left(N_{dn}+N_{ap}\right)^2\left(V_{bi}+V_R\right)}{eN_{ap}N_{dn}\left(\varepsilon_nN_{dn}+\varepsilon_pN_{ap}\right)}\right]^{1/2}. \tag{7}$$

The parameters X_N, X_P, ε_n, ε_p, N_{dn}, N_{ap}, V_{bi}, and V_R correspond to the depletion layer width of the n-type Si layer, the depletion layer width of p-type rubrene film, the Si dielectric constant ($\sim1.05315\times10^{-12}$ F/cm), the rubrene dielectric constant ($\sim2.84\times10^{-13}$ F/cm), the impurity concentration of Si

layer, the impurity concentration of rubrene, the built-in potential of heterojunction (~0.36 V), and the applied bias voltage, respectively. Herein, the resistivity of the n-type Si substrate is 1–3 Ω·cm, thus the parameter N_{dn} is estimated to be $\sim 5 \times 10^{15}$ cm^{-3} at room temperature. The electrical conductivity (σ) of rubrene films is about 0.33×10^2 Ω^{-1}·cm^{-1}, and the hole mobility (μ_p) is estimated to be 40.0 cm^2·V^{-1}·s^{-1}, therefore, according to the equation[19,42,60]

$$\sigma = N_{ap} e \mu_p, \tag{8}$$

the parameter N_{ap} for rubrene films is estimated to be 5.15×10^{18} cm^{-3}. At thermal equilibrium state, the applied bias voltage of V_R is equal to zero, so we can estimate that the width of the space charge region of the heterojunction is about 306.9 nm. However, under the applied bias voltage of −2.0 V, the width of the space charge region increases to 787.3 nm. Therefore, the applied reverse bias voltage can enhance the width of the space charge region of the heterojunction significantly. According to the present theoretical and experimental analysis, this band alignment configuration is more conducive to improve the efficiency of optoelectronic devices. The electrons and holes within the excited state can transfer across the heterojunction interface along two opposite directions, and thus be separated in the two different rubrene and Si layers due to the band offset. Therefore, under the conditions of monochromatic light illumination, the electrons of rubrene films can be stimulated to the energy levels above the LUMO from the HOMO, thus generating electron-hole pairs with much longer lifetime inside the depletion region of the heterostructure devices. Finally, these photoexcited electrons and holes may be driven in the opposite transport directions in these type-Ⅱ heterostructures, as shown in Fig. 8(c). The photoexcited electrons will flow cross the heterojunction interface and then into the silicon layer with n-type background carriers, while the photoexcited holes will move into the rubrene layer with p-type majority carriers. As a result, a discernible photocurrent will be generated in the photodetector, which allows the device to be operated at zero bias voltage as well. This feature is very useful for the state-of-the-art device applications with lower energy consumption. In addition, the band alignment of the rubrene/Si heterostructures can be precisely tuned by introducing an external bias voltage, and Fig. 8(d) shows the regulation mechanism of the applied reverse bias voltage on our heterostructure band alignment. The applied reverse bias voltage can induce an additional potential barrier along the direction of the built-in potential, which can realize a more perfect type-Ⅱ band alignment of the heterostructure and make the device more beneficial for the separation of photoexcited carriers in different layers with further shorten transit time. This also revealed the internal mechanism for the enhanced photoelectric conversion effect for our rubrene/Si heterojunction photodetector operated under external biases, including these important parameters such as photocurrent, responsivity, and detectivity as shown in Fig. 5.

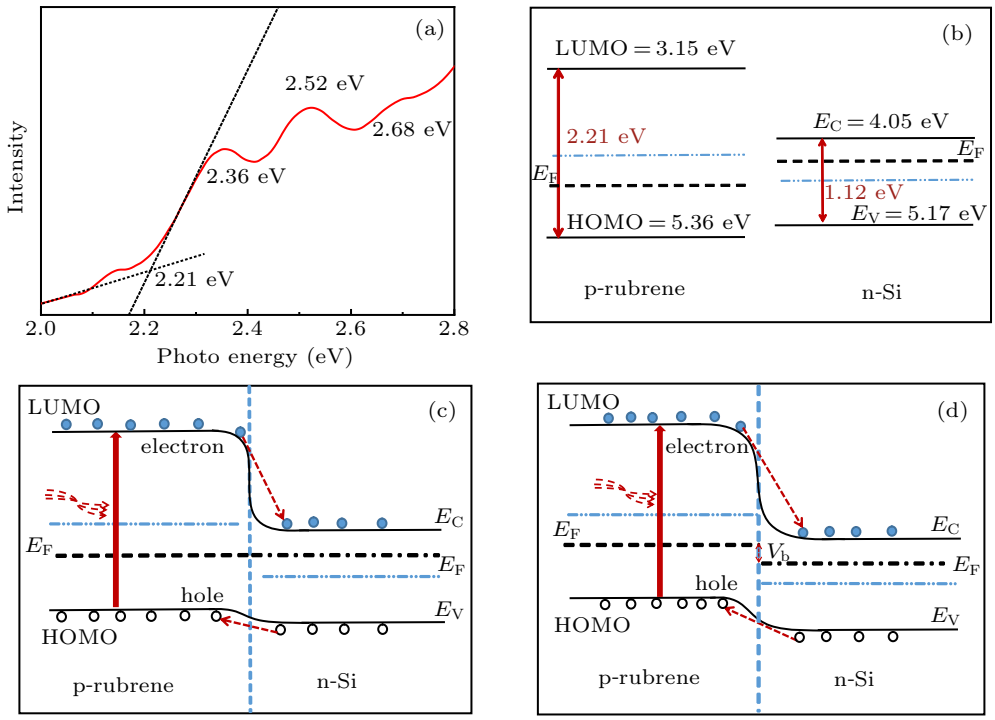


Fig. 8. (a) UV-vis absorption spectrum of rubrene films performed at room temperature. (b) Energy band diagrams of rubrene films and monocrystalline Si. (c) Band alignment of rubrene/Si heterostructures at thermal equilibrium state. (d) Band alignment configuration of rubrene/Si heterostructures tuned by a reverse bias voltage.

3. Conclusion

In summary, we have prepared the high-quality organic/inorganic hybrid van der Waals heterostructures of rubrene/Si with a type-Ⅱ band alignment based on the p-type rubrene crystal films and n-type Si wafers. The as-grown rubrene/Si heterojunction is very beneficial for the photoexcited charge generation and transfer, which can be utilized for the construction of multifunctional photodetectors. Therefore, based on this hybrid heterojunction, the self-powered photodetector that can be operated at zero bias voltage has been successfully fabricated, which demonstrates an excellent switching characteristic to the 1064 nm light with large $I_{\text{photo}}/I_{\text{dark}}$ ratio as high as 7.0×10^3. The output photocurrent can increase to 14.62 mA at −5 V from 0.22 mA at 0 V, and the characteristic parameters of responsivity and detectivity can reach up to 2.07 A/W and 2.9×10^{11} Jones, respectively. In addition, the as-fabricated rubrene/Si heterojunction device can track optical signals with frequency up to 5.0 kHz and show extremely short response time of 13.0 μs, indicating the great potential of high-speed light harvesting and photodetection applications. This study offers important guidance for preparing two-dimensional organic/inorganic hybrid van der Waals heterostructures of rubrene/Si with desirable and staggered band alignment, and the as-fabricated rubrene/Si heterostructure photodetector demonstrates the extensive application prospects especially in multifunctional optoelectronics.

References

[1] Yang T F, Wang X and Zheng B Y 2019 *ACS Nano* **13** 7996
[2] Hu W and Yang J L 2017 *J. Mater. Chem. C* **5** 12289
[3] Fu H Y, Sun F, Liu R, Suo Y Q, Bi J J, Wang C K and Li Z L 2019 *Phys. Lett. A* **383** 867
[4] Shin G H, Park C, Lee K J, Jin H J and Choi S Y 2020 *Nano Lett.* **20** 5741
[5] Novoselov K S, Mishchenko A, Carvalho A and Castro Neto A H 2016 *Science* **353** aac9439
[6] Tran M D, Kim H, Kim J S, Doan M H, Chau T K, Vu Q A, Kim J H and Lee Y H 2019 *Adv. Mater.* **31** 1807075
[7] Liu J, Ma Y Q, Dai Y W, Chen Y, Li Y, Tang Y N and Dai X Q 2019 *Chin. Phys. B* **28** 107101
[8] Gobbi M, Orgiu E and Samorì P 2018 *Adv. Mater.* **30** 1706103
[9] He D W, Pan Y M, Nan H Y, Gu S, Yang Z Y, Wu B, Luo X G, Xu B C, Zhang Y H, Li Y, Ni Z H, Wang B G, Zhu J, Chai Y, Shi Y and Wang X R 2015 *Appl. Phys. Lett.* **107** 183103
[10] Liu Y, Huang Y and Duan X F 2019 *Nature* **567** 323
[11] Wu F, Xia H, Sun H D, Zhang J W, Gong F, Wang Z, Chen L, Wang P, Long M S, Wu X, Wang J L, Ren W C, Chen X S, Lu W and Hu W D 2019 *Adv. Funct. Mater.* **29** 1900314
[12] Zheng W H, Zheng B Y and Jiang Y *et al.* 2019 *Nano Lett.* **19** 7217
[13] Zhang L L, Sharma A, Zhu Y, Zhang Y H, Wang B W, Dong M H, Nguyen H T, Wang Z, Wen B, Cao Y J, Liu B Q, Sun X Q, Yang J, Li Z Y, Kar A, Shi Y, Macdonald D, Yu Z F, Wang X R and Lu Y R 2018 *Adv. Mater.* **30** 1803986
[14] Bellus M Z, Li M, Lane S D, Ceballos F, Cui Q N, Zeng X C and Zhao H 2017 *Nanoscale Horiz.* **2** 31
[15] Zhang K A, Zhang T N, Cheng G H, Li T X, Wang S X, Wei W, Zhou X H, Yu W W, Sun Y, Wang P, Zhang D, Zeng C G, Wang X J, Hu W D, Fan H J, Shen G Z, Chen X, Duan X F, Chang K and Dai N 2016 *ACS Nano* **10** 3852
[16] Wang Y J, Wang L, Liu F J, Peng Z H, Zhang Y D and Jiang C 2020 *Org. Electron.* **83** 105778
[17] Sun J, Choi Y, Choi Y J, Kim S, Park J H, Lee S and Cho J H 2019 *Adv. Mater.* **31** 1803831
[18] Zhu L B, Lu L, Wang H Y, Fan G C, Chen Y T, Zhang J D and Zhao W W 2019 *Biosens. Bioelectron.* **140** 111349
[19] Borges-González J, Kousseff C J and Nielsen C B 2019 *J. Mater. Chem. C* **7** 1111
[20] Fahlman M, Fabiano S, Gueskine V, Simon D, Berggren M and Crispin X 2019 *Nat. Rev. Mater.* **4** 627
[21] Li D, Dong G F, Li W Z and Wang L D 2015 *Sci. Rep.* **5** 07902
[22] Wu Y L, Fukuda K, Yokota T and Someya T 2019 *Adv. Mater.* **31** 1903687
[23] Fusella M A, Schreiber F, Abbasi K, Kim J J, Briseno A L and Rand B P 2017 *Nano Lett.* **17** 3040
[24] Reyes-Martinez M A, Ramasubramaniam A, Briseno A L and Crosby A J 2012 *Adv. Mater.* **24** 5548
[25] Chung S J, McHugh C J and Calvo-Castro J 2019 *J. Mater. Chem. C* **7** 2029
[26] Irkhin P, Ryasnyanskiy A, Koehler M and Biaggio I 2012 *Phys. Rev. B* **86** 085143
[27] Gogoi D, Hussain A A, Biswasi S and Pal A R 2020 *J. Mater. Chem. C* **8** 6450
[28] Zhao Y P, Yu W B and Ouyang G 2018 *J. Phys. D: Appl. Phys.* **51** 015111
[29] Zheng W H, Zheng B Y, Yan C L, Liu Y, Sun X X, Qi Z Y, Yang T F, Jiang Y, Huang W, Fan P, Jiang F, Ji W, Wang X and Pan A L 2019 *Adv. Sci.* **6** 1802204
[30] Udhardt C, Forker R, Gruenewald M, Watanabe Y, Yamada T, Ueba T, Munakata T and Fritz T 2016 *Thin Solid Films* **598** 271
[31] Lin K Y, Wang Y J, Chen K L, Ho C Y, Yang C C, Shen J L and Chiu K C 2017 *Sci. Rep.* **7** 40824
[32] Djuric T, Thierry A, Grogger W, Abd Al-Baqi S M, Sitter H and Resel R 2009 *Physica E* **41** 1718
[33] Wang C H, Islam A K M M, Yang Y W, Wu T Y, Lue J W, Hsu C H, Sinha S and Mukherjee M 2013 *Langmuir* **29** 3957
[34] Zhang P Q, Zeng X H, Deng J C, Huang K, Bao F, Qiu Y X, Xu K and Zhang J P 2010 *Jpn. J. Appl. Phys.* **49** 095501
[35] Singh N, Arish M, Kumar P, Rub A and Riaz U 2020 *Sci. Rep.* **10** 57
[36] Goldie D M and Persheyev S K 2006 *J. Mater. Sci.* **41** 5287
[37] Orduña-Diaz A, Treviño-Palacios C G, Rojas-Lopez M, Delgado-Macuil R, Gayou V L and Torres-Jacome A 2010 *Mater. Sci. Eng. B* **174** 93
[38] Zhou X W, Ishida M, Imanishi A and Nakato Y 2001 *J. Phys. Chem. B* **105** 156
[39] Strauss I, Chakarova K, Mundstock A, Mihaylov M, Hadjiivanov K, Guschanski N and Caro J 2020 *Microporous Mesoporous Mater.* **302** 110227
[40] Uddin A, Lee C B and Wong J 2011 *J. Lumin.* **131** 1037
[41] Goto K, Takayama T, Ohata K, Matsushita K and Akimoto I 2019 *J. Lumin.* **205** 46
[42] Burke F, Stamenov P and Coey J M D 2011 *Synth. Met.* **161** 563
[43] Liu C, Zhang H B, Sun Z, Ding K, Mao J, Shao Z B and Jie J S 2016 *J. Mater. Chem. C* **4** 5648
[44] Xie C, Liu C K, Loi H L and Yan F 2019 *Adv. Funct. Mater.* **30** 1903907
[45] Sun L, Wang L, Lu J L, Liu J, Fang J, Xie L L, Hao Z B, Jia H Q, Wang W X and Chen H 2018 *Chin. Phys. B* **27** 047209
[46] Chowdhury A M, Chandan G, Pant R, Roul B, Singh D K, Nanda K K and Krupanidhi S B 2019 *ACS Appl. Mater. Interfaces* **11** 33390
[47] Liu B, Tang B, Lv F J, Zeng Y, Liao J H, Wang S and Chen Q 2019 *Nanotechnology* **31** 065203
[48] Liu Q R, Jian L H, Liu R Q, Yang H X, Kong J M and Zhang X J 2020 *Chem. Eur. J. A* **26** 1633
[49] Kielar M, Hamid T, Wiemer M, Windels F, Hirsch L, Sah P and Pandey A K 2019 *Adv. Funct. Mater.* **30** 1907964
[50] Zhu W G, Zhang D Z, Bai S M, Shi Q, Hu W P and Fu H B 2020 *Adv. Opt. Mater.* **8** 2000866
[51] Cho E H, Song W G, Park C J, Kim J, Kim S and Joo J 2015 *Nano Res.* **8** 790
[52] Jones G F, Pinto R M, De Sanctis A, Nagareddy V K, Wright C D, Alves H, Craciun M F and Russo S 2017 *Adv. Mater.* **29** 1702993
[53] Biswasi S and Pal A R 2019 *Plasma Chem. Plasma Process.* **40** 371
[54] Du Q Q, Qin S C, Wang W J, Guo Y Y, Ye J D, Zhu S M, Tang K, Zhang R, Zheng Y D and Gu S L 2019 *Nanotechnolgy* **30** 065202
[55] Huang J, Wang L J, Tang K, Xu R, Zhang J J, Lu X G and Xia Y B 2011 *Chin. Phys. Lett.* **28** 127301
[56] Wang Z K, Naka S and Okada H 2010 *Appl. Phys. A* **100** 1103
[57] He X X, Chow W L, Liu F C, Tay B K and Liu Z 2017 *Small* **13** 1602558
[58] Fan H J, Zhang H Q, Wu J J, Wen Z F and Ma F Y 2011 *Chin. Phys. Lett.* **28** 127305
[59] Zhao Y P and Ouyang G 2019 *Sci. Rep.* **9** 17381
[60] Zhang H B, Yao J D, Shao J M, Li H, Li S W, Bao D H, Wang C X and Yang G W 2014 *Sci. Rep.* **4** 05876